RESEARCH ARTICLE

A wear-resistant metastable CoCrNiCu high-entropy alloy with modulated surface and subsurface structures

Yue REN[1], Qian JIA[1], Yin DU[1], Qing ZHOU[1,*], Christian GREINER[2], Ke HUA[1], Haifeng WANG[1,*], Jian WANG[3]

[1] *State Key Laboratory of Solidification Processing, Center of Advanced Lubrication and Seal Materials, Northwestern Polytechnical University, Xi'an 710072, China*

[2] *Institute for Applied Materials, Karlsruhe Institute of Technology, Karlsruhe 76131, Germany*

[3] *Mechanical and Materials Engineering, University of Nebraska-Lincoln, Nebraska 68588, USA*

© The author(s) 2022.

Abstract: Sliding friction-induced subsurface structures and severe surface oxidation can be the major causes influencing the wear resistance of ductile metallic materials. Here, we demonstrated the role of subsurface and surface structures in enhancing the wear resistance of an equiatomic metastable CoCrNiCu high-entropy alloy (HEA). The CoCrNiCu HEA is composed of a CoCrNi-rich face-centered cubic (FCC) dendrite phase and a Cu-rich FCC inter-dendrite phase. Copious Cu-rich nano-precipitates are formed and distributed uniformly inside the dendrites after tuning the distribution and composition of the two phases by thermal annealing. Although the formation of nano-precipitates decreases the hardness of the alloy due to the loss of solid solution strengthening, these nano-precipitates can be deformed to form continuous Cu-rich nanolayers during dry sliding, leading to a self-organized nano-laminated microstructure and extensive hardening in the subsurface. In addition, the nano-precipitates can facilitate the formation of continuous and compacted glaze layers on the worn surface, which are also beneficial for the reduction of the wear rate of CoCrNiCu. The current work can be extended to other alloy systems and might provide guidelines for designing and fabricating wear-resistant alloys in general.

Keywords: high-entropy alloys (HEA); wear; nano-laminated structure; oxidation; atomic force microscope (AFM)

1 Introduction

High/medium-entropy alloys (HEAs/MEAs) are composed of multiple principal elements in equiatomic or near-equal atomic ratios. Over the past few years, CoCrNi-based alloys have served as the prime example of MEAs with a single FCC crystal structure [1, 2]. Numerous studies have shown excellent properties of CoCrNi-based alloys, including superior combination of strength and ductility, damage tolerance at cryogenic temperature, good thermal stability, radiation and corrosion resistance [3–7]. Challenges in utilizing CoCrNi-based alloys as structural materials are primarily their low yield strength and poor wear resistance [5, 8, 9]. Although the mechanical properties have been extensively investigated [10–12], limited resources have been directed towards the evaluation of more complex mechanical loading such as friction and wear [8, 13].

Pursuing the development of materials with high wear resistance has been a lasting endeavor as such alloys are important for the reliability and durability of many components, especially for those which cannot be easily replaced under critical service conditions. There are several factors affecting the wear resistance of materials. First, the wear resistance is highly related to the material's intrinsic features, such as microstructures, compositions, surface states,

---

* Corresponding authors: Qing ZHOU, E-mail: zhouqing@nwpu.edu.cn; Haifeng WANG, E-mail: haifengw81@nwpu.edu.cn

mechanical properties, and thermal stability properties [14–18]. Second, the tribological behavior is a dynamic evolution process during service. The oxidation of the worn surface, the evolution of the subsurface microstructure, and the deformation induced hardening of materials will constantly affect the tribological properties of a material [19–22]. Consequently, it has been suggested that the materials loss can be rationalized once one understands and is able to describe the surface and subsurface evolution as well as the third-body behavior [23]. Thus, well-designed and controlled surface and subsurface holds the prospect for improving the tribological properties. Yin et al. [24] reported that a self-lubricating layer composed of nano-oxide particles and amorphous oxide is responsible for the low friction and wear of a specific carbon steel alloy. Dreano et al. [25] investigated the structure of the protective glaze layer formed during a fretting wear process. Chen et al. [26] reported that a stable gradient nanostructure of Cu alloy can accommodate large plastic strains under repeated sliding and enables a significant reduction in the friction coefficient and wear loss. Greiner et al. [27] elucidated the elementary mechanisms for the transformation of subsurface microstructures by systematic model experiments and discrete dislocation dynamics simulations in dry frictional contacts. These studies have all recognized that sliding friction dramatically changes the initial service status, thus resulting in the formation of tribolayers and the friction-induced subsurface structure which in turn have a huge influence on the materials' tribological properties. However, for HEA, such understanding is still insufficient despite its significance for the design of wear-resistance alloys.

To this end, CoCrNi-based alloy is chosen as prototypical materials in this work to explore the subsurface microstructure and tribo-layer formation and how they feed back on friction and wear properties of HEA. We report on the development of a metastable equiatomic CoCrNiCu HEA to enhance the poor wear resistance. The addition of Cu was motivated by the formation of wear-resistant CuO during friction. The equiatomic CoCrNiCu HEA is composed of a CoCrNi-rich FCC dendrite phase and a Cu-rich FCC inter-dendrite phase. By tuning the annealing conditions, copious Cu-rich nano-precipitates form and distribute uniformly inside the dendrites, which can be further deformed to form continuous Cu-rich nanolayers during dry sliding, leading to a self-organized nano-laminated microstructure. These Cu-rich nanolayers can provide an extensive hardening effect and significantly improve the wear resistance. The current work is expected to obtain an in-depth understanding of the wear mechanisms active in dual-phase HEAs and shed light on a promising approach for designing wear-resistant materials.

2 Experiments

2.1 Material preparation and microstructure characterization

The ingots with a nominal composition of CoCrNiCu were prepared by the arc-melting using bare metals with a purity better than 99.9 wt%. For a Ti-gettered argon atmosphere, pure titanium was melted for 3 min to ensure adequate consumption of residual oxygen in cavity. Subsequently, the ingots were re-melted for five times to ensure homogeneity. Plate-like ingots (named as the as-cast samples hereafter) were fabricated by copper mold casting with a size of 5 mm × 15 mm × 60 mm. The as-cast samples were thermally annealed in vacuum quartz tubes (with vacuum degree less than 1×10^{-2} Pa) at 1,100 °C for 6, 24 or 45 h and subsequently quenched in water (named as the A-6h, A-24h, and A-45h samples hereafter). The microstructure and composition were characterized by scanning electron microscope (SEM, FEI Helios G4 CX) and energy dispersive spectroscope (EDS, Oxford X-Max^{N}). The phases of the samples were identified by X-ray diffraction (XRD, Bruker D8) with Cu Kα radiation (λ = 1.54060 Å), scanning from 20° to 100° with the scanning speed is 2.8 (°)/min. The Vickers microhardness measurements were conducted under a load of 500 gf with a dwell time of 15 s, an indentation dot matrix of 3×3 was performed in a random selected area of 3 mm × 3 mm.

2.2 Wear tests and characterization

Reciprocating dry sliding wear tests were performed on a lab tribometer (Rtec MFT-5000) against a hardened

steel ball (GCr15) under the normal loads of 5 and 10 N. The diameter and Vickers hardness of the GCr15 balls are 6.35 mm and 600±20 HV, respectively. The stroke length, reciprocating frequency, and sliding time were fixed as 2 mm, 3 Hz, and 15 min, respectively. The samples for wear tests were ground using 200, 800, 2,000, 4,000 grit sandpaper and mechanically polished using 2.5 μm diamond paste to ensure the surface roughness less than 5 nm (verified by atomic force microscope (AFM)). The wear losses were calculated from three-dimensional (3D) whitelight profilometry (Bruker Contour GT-K1) of the worn samples. The morphology of the worn surfaces was examined by SEM, and X-ray photoelectron spectroscopy (XPS, PHI 5000 VersaProbe III) with monochromatic Al Kα radiation was applied to analyze the chemical state of elements on the worn surface. Foils for transmission electron microscopy (TEM) were prepared by focused ion beam (FIB) using a standard lift-out technique. High-resolution TEM (HRTEM) and high-angle annular dark-field scanning transmission electron microscopy (HAADF- STEM) coupled with EDS (FEI Talos F200X) were applied to observe the microstructure beneath the worn surface. Transmission Kikuchi diffraction (TKD) possesses a higher spatial resolution (e.g., in the scale of 2–10 nm for a range of materials [28]) when compared with conventional technique of electron backscattered diffraction (EBSD). To characterize the nanoscale structures beneath the worn surface which have undergone severe deformation, the samples with a thickness of 80–100 nm for TKD experiments were prepared by FIB. The TKD analysis was performed with an SEM (FEI Helios G4 CX) equipped with an EBSD detector (Oxford Nordlys Nano) using an accelerating voltage of 20 kV with a step size of 1.5 nm.

2.3 AFM indentation test

AFM-based indentation (Oxford MFP-3D Origin+) with an indentation area in nanoscale was applied to measure the local hardness distribution beneath the worn surface. An area of 3 μm × 3 μm in the cross-section was chosen. Before the indentation was performed, the sample were ground and mechanically polished as described above. Vibration polishing was applied for 5 h with an alumina suspension of 0.05 μm,

to exclude the preparation artefacts and ensure that the roughness was less than 3 nm. Tapping mode was applied to find the target 3 μm × 3 μm area and maximally protect the tip from damage due to imaging. When the target 3 μm × 3 μm area was found where it is located as close as possible to the worn surface (less than 200 nm), contact mode was initialized to conduct the indentation testing. Quantitative nanoscale mechanical characterization was carried out using cantilever with a single-crystalline diamond tip (Adama AD-40-AS). The radius at the top of the tip provided by the manufacturer is 10±5 nm, and the spring constant of the cantilever is measured to be ~36.86 nN/nm by the thermal tuning method [29]. The maximum force was 500 nN to ensure that the indentation depths do not exceed the tip length, and the dwell time was set to 1 s to ensure the stability. The indentation hardness is calculated by fitting the force curve with the Derjaguin-Muller-Toporov (DMT) model [30–32]. Accordingly, the spatial distribution of nano-hardness for each sample was obtained from a dot matrix of 20 × 20 in the selected area of 3 μm × 3 μm. Here, the dot spacing was set to be 150 nm to exclude the influences between adjacent indentations.

3 Results

3.1 Microstructure

Figure 1(a) shows the microstructure of the as-cast CoCrNiCu HEA, which is made up of typical dendrite and inter-dendrite phases. The element distribution is shown in Fig. 1(b). It is clearly that the Co, Cr, and Ni contents are nearly constant inside the dendrites, whereas the composition of Cu increases dramatically from 10 at% to 70 at% when scanning from the dendrite into the inter-dendrite region. A higher magnification image of the inter-dendrite phase and the corresponding EDS elemental mappings are shown in Fig. 1(c). Co, Cr, and Ni distribute homogeneously in the dendrites, whereas Cu prefers to segregate to the inter-dendrites due to its positive enthalpy of mixing with all the other elements. It's noted that there is still a portion of Cu (about 10 at%) concentrated in the dendrites and thus exhibits a metastable state, which is important for the Cu-rich precipitation after subsequent annealing.
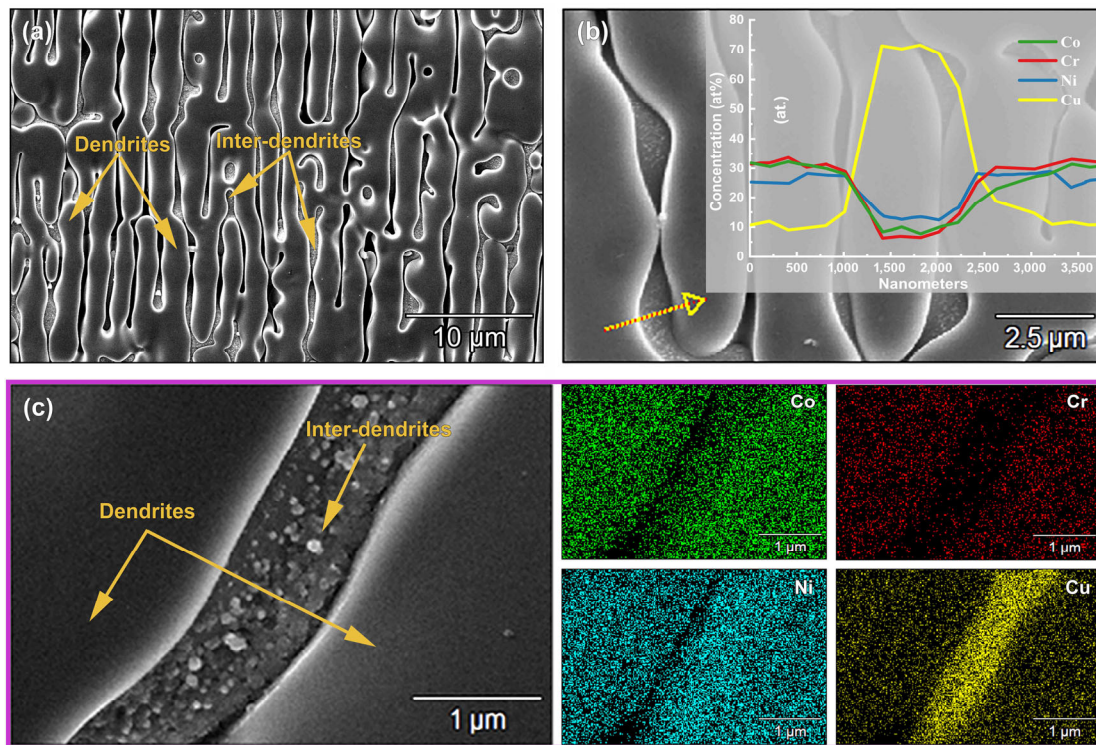
Fig. 1 (a) Microstructure of the as-cast CoCrNiCu HEA; (b) element content variations from the dendrite phase to the inter-dendrite phase, which is taken from the line indicated by the yellow arrow; and (c) higher magnification image of inter-dendrite phase and corresponding EDS mappings.

Figures 2(a)–2(d) shows the microstructures of the samples with different annealing time. It is obvious that the grain size does not change with the increasing annealing time. Especially for the A-45h sample, it can be found that there is a significant proportion of precipitates inside the dendrites as shown by the enlarged microstructure in Fig. 2(e). It is noteworthy that the size of precipitates is less than 100 nm, which might be a result of sluggish diffusion of Cu in the multi-principle alloys that restricts phase growth [33]. To further analyze the difference between the as-cast and the A-45h samples, XRD analysis is applied and shown in Fig. 2(f). The structure of both alloys includes two FCC phases, i.e., the major CoCrNi-rich MEA matrix and the minor Cu-rich precipitates. The corresponding TEM and corresponding EDS mappings are given in Fig. S1 in the Electronic Supplementary Material (ESM), which reveals that the precipitates are rich in Cu element. Compared with the as-cast sample, the peak of Cu-rich phase in the A-45h sample exhibits a higher intensity, indicating a higher proportion.

The Vickers hardness and Cu content of CoCrNiCu HEA with different annealing times are plotted in Fig. 3. It shows that the Cu content decreases in the dendrites with annealing time, in accordance with the precipitation of Cu. The Vickers hardness of all the samples does not exceed 190 HV, indicating the relative soft nature of the CoCrNiCu HEA. The maximum average hardness of 179.2 HV is obtained by the as-cast sample. The A-45h sample owns the minimum average Vickers hardness of 153.2 HV, showing approximately a 14.5% reduction. As the annealing time increases, soft Cu phase precipitates from the dendrites. The weakening of the solution strengthening could be responsible for the reduction of the strength and hardness of this HEA.

3.2 Tribological performance

A series of dry sliding wear tests under 5 and 10 N are applied to the CoCrNiCu HEA. Figure 4 plots the results for the friction coefficient and wear rate. In Fig. 4(a), the friction coefficients show a similar tendency, i.e., after an initial run-in state, they become
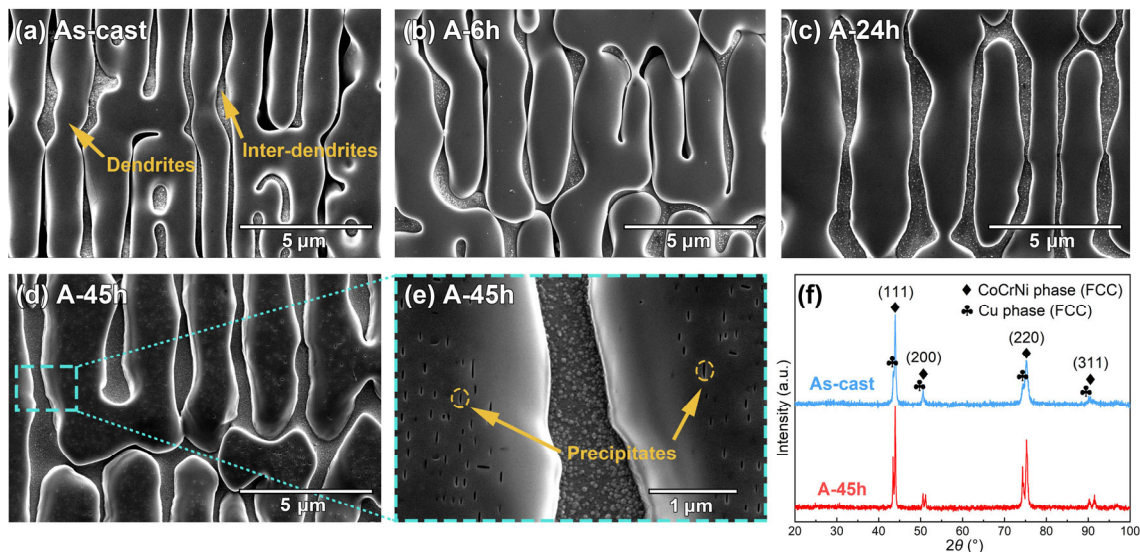
Fig. 2 (a–d) Microstructure of the CoCrNiCu HEA with annealing times of 0, 6, 24, and 45 h, respectively; (e) higher magnification of microstructure as indicated by the box in (d) of the A-45h sample; (f) XRD analyses of the as-cast and the A-45h samples.
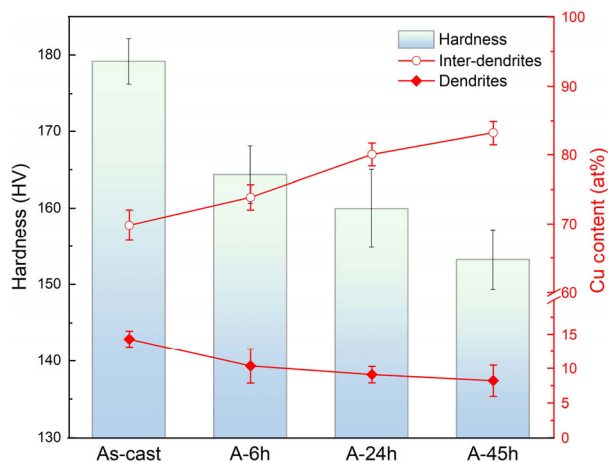

Fig. 3 The Vickers hardness of the CoCrNiCu HEA alloys after thermal annealing and corresponding Cu content of the dendrite and the inter-dendrite phases.

stable at about 0.65 under both normal forces of 5 and 10 N. From Fig. 4(b), the calculated wear rate of the alloys under 5 and 10 N monotonously decreases with the annealing time. For example, the wear rate under 5 N decreases from 5.6×10^{-5} $mm^3/(N\cdot m)$ of the as-cast sample to 2.9×10^{-5} $mm^3/(N\cdot m)$ of the A-45h sample, i.e., a reduction of about 48.2%. Similarly, the wear rate under 10 N decreases from 5.4×10^{-5} to 2.3×10^{-5} $mm^3/(N\cdot m)$, i.e., a reduction of 57.4%. It should be mentioned that the wear rate under 10 N is slightly lower than that under 5 N. Lower wear rate under higher stress is generally reported in ductile materials [34–36], that high stress induced sufficient

oxidation and strain hardening effect are believed responsible for the decreased wear rate. Meanwhile, the A-45h sample owns the best wear resistance, even though its hardness is lowest, the detailed reasons will be discussed in Section 4.

Figures 5(a) and 5(b) show the typical wear morphologies of the as-cast and the A-45h samples under 10 N. Panels (I) and (II) present the magnified wear morphologies and the corresponding EDS mappings of oxygen. The as-cast sample presents typical abrasive and adhesive wear as shown in Fig. 5(a). Ploughing grooves are parallel to each other and extend throughout the entire wear track length. Meanwhile, a large amount of debris, cracks, and peeling-off of the tribolayers appear on the worn surface. In contrast, for the A-45h sample in Fig. 5(b), the wear mechanisms are abrasive and oxidation wear. Except for the typical grooves on the worn surface, a large amount of dark scales is formed on the surface. The EDS mapping reveals that these dark patches on the worn surface of the A-45h sample contain a much higher amount of oxygen (25.7 at%) than the as-cast sample (4.5 at%). These glaze layers are originated from the compaction of wear debris and severe oxidation, which is found beneficial to the wear resistance due to its high hardness [37–39].

To further analyze the tribolayers, XPS analysis on the worn surface of the as-cast and the A-45h samples were carried out with the results presented in
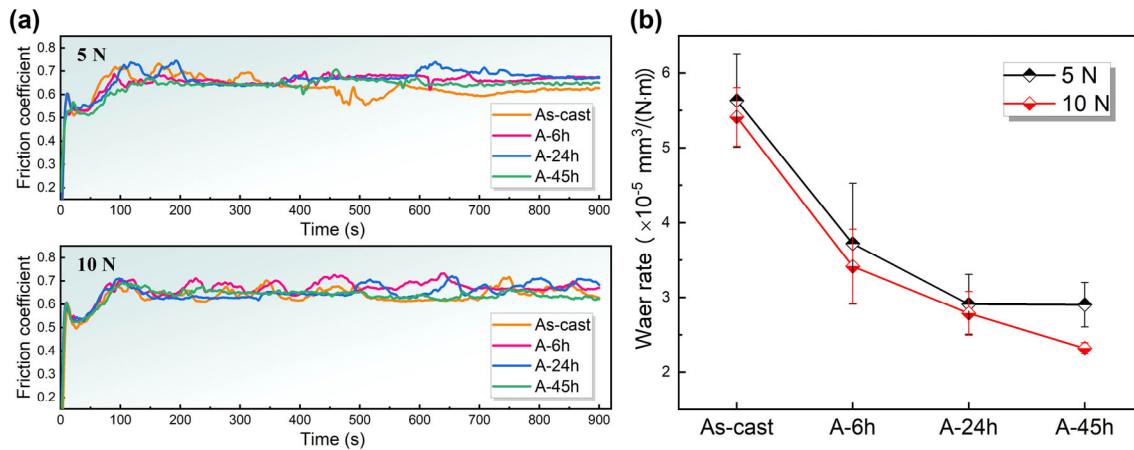
Fig. 4 Wear characteristics of the CoCrNiCu HEA under two normal forces of 5 and 10 N. (a) Friction coefficients as a function of the sliding time and (b) wear rates for different samples.
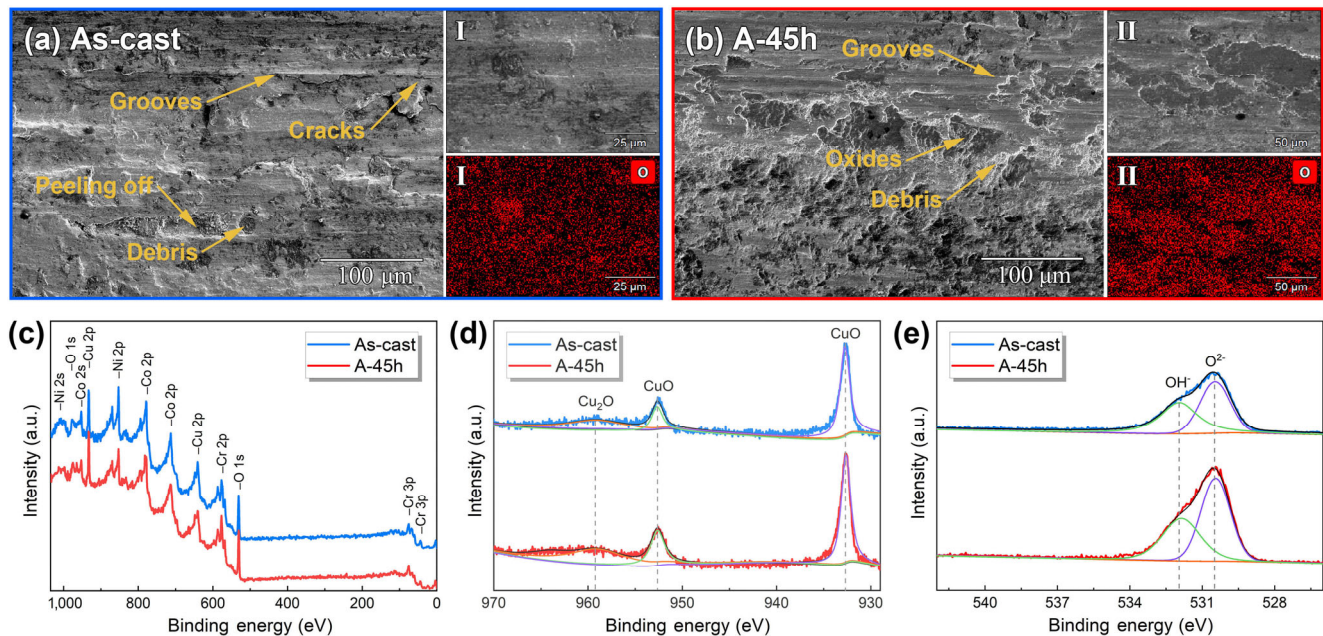

Fig. 5 (a, b) Typical wear morphologies under a normal force of 10 N of the as-cast and the A-45h samples; regions (Ⅰ) and (Ⅱ) are the magnified wear morphologies and corresponding EDS mappings for oxygen; (c–e) XPS analysis on the tribolayers of the as-cast and the A-45h samples, including (c) survey spectrums and (d, e) high-resolution XPS spectra of Cu and O.

Figs. 5(c)–5(e). In Fig. 5(c), the XPS survey spectra covers a wide binding energy range, which consists the main peaks of Co 2s, Co 2p, Cr 2p, Cr 3p, Ni 2s, Cu 2p, and O 1s. In Figs. 5(d) and 5(e), the high-resolution XPS spectra shows clear peaks of Cu oxides, suggesting that the tribolayers contain CuO and Cu_2O. Compared with the as-cast sample, the total amount of oxide in the A-45h sample increases as evidenced by the peak intensity of Cu^+, Cu^{2+}, and O^{2-}, which agrees with the above EDS analysis.

3.3 Characteristic microstructures of subsurface

To further investigate the wear mechanism, FIB was applied to lift out TEM foils located in the middle of the worn surface, to perform detailed microstructural characterization. Figure 6(a) exhibits the overall cross-section beneath the worn surface of the as-cast sample. A typical friction-induced microstructure is formed, which contains three characteristic regions, i.e., the severely deformed region (SDR), the slightly
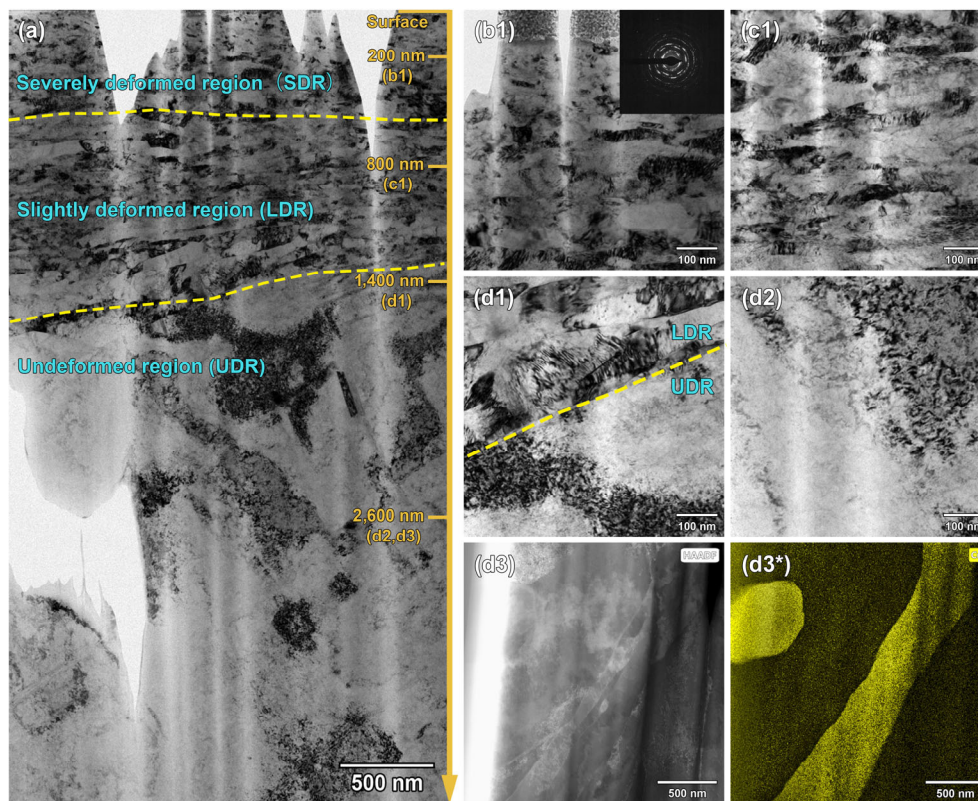
Fig. 6 Cross-sectional TEM micrographs beneath the worn surface of the as-cast sample. (a) Overall bright-field TEM micrograph of the as-cast sample showing three typical regions: SDR, LDR, and UDR. High-magnification bright-field TEM images of (b1) SDR, (c1) LDR, (d1) the boundary between the LDR and UDR, and (d2) the UDR. (d3, d3*) High-angle annular dark field-scanning transmission electron microscopy (HAADF-STEM) and the corresponding energy dispersive spectroscope (EDS) map of Cu in the UDR.

deformed region (LDR), and the undeformed region (UDR). Figure 6(b1) shows the SDR of the as-cast sample, where a nanoscale polycrystalline region with a depth extending to 500 nm from the surface can be identified. The grains inside this region are equiaxed or near-equiaxed without strong texture, and the topmost grain size is no larger than 10 nm. A coarser grain size is obtained away from the worn surface, exhibiting a gradient structure with the increasing depth. From the selected-area electron diffraction (SAED) pattern, the diffraction spots show typical polycrystalline characteristics. In Fig. 6(c1), friction-induced elongated grains form a nanolayered structure of the LDR, which extend along the sliding direction with a depth reaching down to 1,200 nm. There is a distinct boundary (yellow dashed line) between the LDR and the UDR as shown in Fig. 6(d1). Figure 6(d2) exhibits the UDR where no obvious deformation and grain refining can be found here, and the microstructure is consistent with the as-cast

sample. In Figs. 6(d3) and 6(d3*), HAADF-STEM and corresponding EDS of Cu show the typical microstructure of Cu-rich inter-dendrite phase in UDR, further demonstrating that no obvious deformation and refinement occurred here.

Figure 7(a) shows the overall cross-section beneath the worn surface of the A-45h sample. There are three typical characteristic regions which is analogous to the as-cast sample, but significant differences can be observed. In Fig. 7(b1), there exists a larger area of SDR in the A-45h sample, the depth of SDR can reach down to 1100 nm. The typical friction-induced nanolayers in the LDR are exhibited in Fig. 7(c1) and the depth of LDR reaches to 2600 nm. Additionally, a large amount of deformation twins inclined to the nano-laminates appear in this region, with the HRTEM image and corresponding diffraction shown in Fig. 7(c2). The UDR in Fig. 7(d1) shows no plastic deformation below a depth of 2600 nm. The HAADF image and the corresponding EDS mapping for Cu
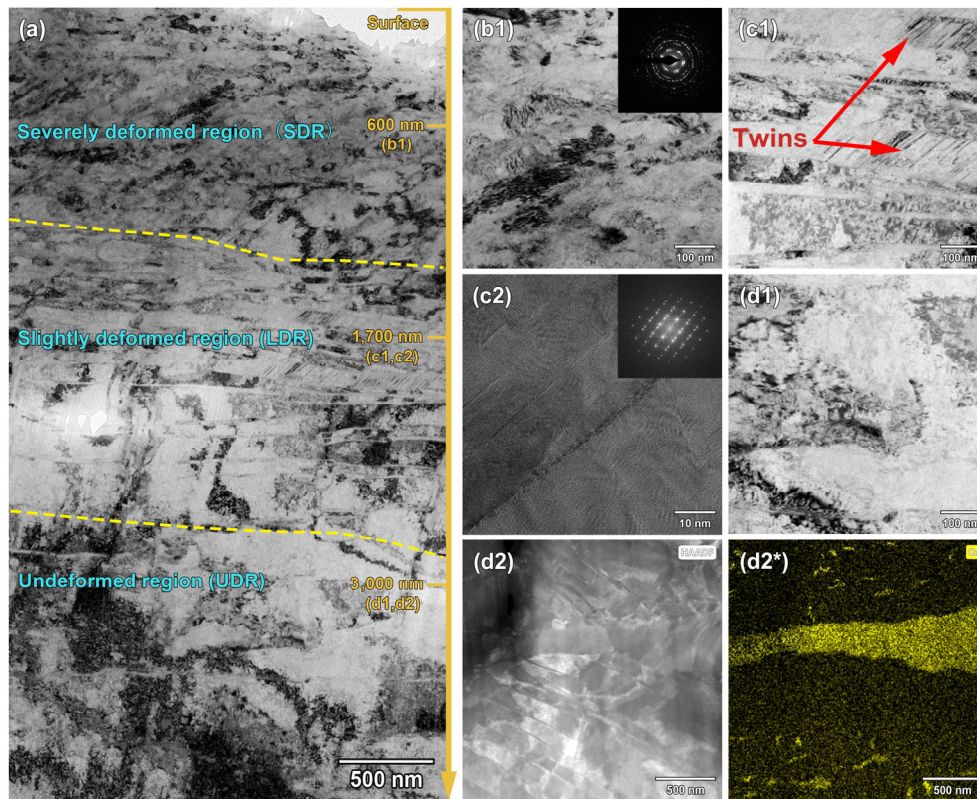
Fig. 7 Cross-sectional TEM micrographs beneath the worn surface of the A-45h sample. (a) Overall bright-field TEM micrograph of the A-45h sample. A high-magnification bright-field TEM images of (b1) the SDR, (c1) the LDR, (c2) high-resolution TEM images of the twins/stacking faults and (d1) the UDR. (d2, d2*) HAADF-STEM and the corresponding EDS map of Cu in UDR.

further present the origin microstructure in Fig. 7(d2, d2*). Apart from the Cu-rich inter-dendrite phase, Cu-rich nano-precipitates within the dendrites can be observed in Fig. 7(d2*) as well.

For the sake of comparison of the two samples, the HAADF-STEM images of subsurface microstructure are shown in Figs. 8(a1) and 8(b1). Both the as-cast and the A-45h samples exhibit sliding friction-induced laminated structures. The EDS mapping of the as-cast sample in Fig. 8(a2) confirms the composition of these chemical layers, i.e., the CoCrNi-rich MEA layers and the thick-Cu layers (to differentiate the thin-Cu nanolayers in the A-45h sample). Furthermore, the thickness of Cu-rich layers shows typical normal distribution ranging between 10–120 nm and the average thickness is 50 nm as shown in Fig. 8(a3). For the A-45h sample, the sliding friction-induced laminated structures are quite different. Beside the CoCrNi-rich MEA layers and thick-Cu layers, a higher density of thin-Cu nanolayers can be observed in Fig. 8(b2). As a result, the thickness of Cu-rich layers

exhibits a bimodal distribution as shown in Fig. 8(b3), with the thickness range of 5–20 nm and 20–120 nm, respectively.

4　Discussion

In this work, the thermal treated A-45h sample shows a reduction of 14.5% in its hardness, while the wear resistance increases by 48.2% and 57.4% under 5 and 10 N, respectively, which is in apparent contradiction with Archard's prediction [40, 41]. We ascribed this improved wear performance to the sliding friction-governed laminated structure and surface oxidation in the CoCrNiCu HEA, which will be discussed further in the following sections.

4.1　Sliding friction-induced laminated structure

To distinguish the mechanical response of the Cu and CoCrNi phases in this work, a stress analysis is required for better investigating the tribological
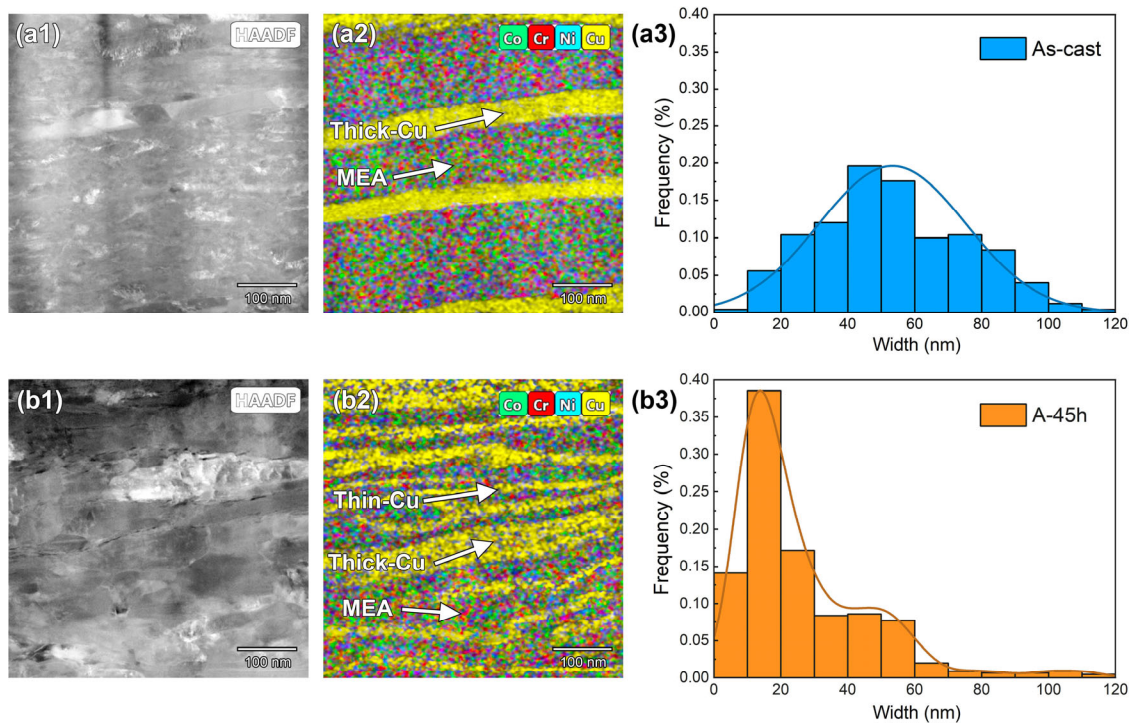
Fig. 8 (a1, b1) HAADF-STEM images and (a2, b2) corresponding EDS mappings of the deformed region of the as-cast sample and the A-45h sample, respectively. (a3, b3) Thickness distribution of Cu-rich nanolayers in the as-cast and the A-45h samples.

behavior. Based on the Hertzian contact model, the maximum contact stress σ_{max} for a sphere-on-plane contact can be approximately estimated as follows [42]:

$$\sigma_{max} = \frac{3P}{2\pi a^2} \tag{1}$$

$$a = \sqrt[3]{\frac{3PR}{4E^*}} \tag{2}$$

$$\frac{1}{E^*} = \frac{1-v_1^2}{E_1} + \frac{1-v_2^2}{E_2} \tag{3}$$

Here $P = 10$ N is the applied normal load, $R = 3.175$ mm is the radius of the hardened GCr15 sphere, E_1, v_1 and E_2, v_2 are the Young's modulus and Poisson's ratio of GCr15 sphere and target material, respectively. For GCr15, Cu, and CoCrNi MEA, their Young's modulus E are 208, 110, 229 GPa, and their Poisson's ratio v are 0.3, 0.34, and 0.31 [5]. Finally, σ_{max} of GCr15-Cu and GCr15-MEA contacts are calculated to be 1.41 and 1.08 GPa, which are far beyond their respective yield strengths of 0.1 and 0.4 GPa [5, 43], and thus both Cu and CoCrNi MEA are expected to plastically deform during sliding. Especially, Cu has a quite low yield strength, but suffers a higher stress when compared

with CoCrNi. Therefore, Cu may bear a higher plasticity during sliding and then influences the friction-induced subsurface structure as discussed in the following.

Both the as-cast and the A-45h samples exhibit a sliding friction-induced nano-laminated structure as presented in Fig. 8. The MEA nanolayers and the thick-Cu are considered to have evolved from the CoCrNi-rich dendrites and Cu-rich inter-dendrites. Particularly, a large amount of thin-Cu nanolayers with a thickness less than 20 nm, which probably originated from the Cu-rich precipitates within the dendrites, can be observed in the A-45h sample. Under the cooperative compression and shear stresses during sliding, the Cu-rich precipitates within the dendrites could be sheared and transformed into the thin-Cu nanolayers, which might significantly promote wear resistance. The prerequisites for the formation of these structure are as follows: First, the initial size of the precipitates needs to be maintained at the nanoscale that the smaller precipitates will be transformed into thinner layers. Second, the precipitates need to be ductile enough, so they can be constantly deformed under the shear stress. Finally, the deformation ability

of the matrix should be consistent with that of the precipitates, and both phases can deform at the same time without brittle failure, such that the formation of cracks and peeling off events are avoided.

To elucidate the deformed structure of the Cu-rich nanolayers, HRTEM was performed on the as-cast and the A-45h samples. Wear induced laminated interfaces between the MEA and the Cu-rich layers are clearly shown in Fig. 9. The interfaces between the thick Cu layer and the MEA are exhibited in Figs. 9(a) and 9(b), and the interfaces between the thin Cu nanolayer and the MEA are shown in Fig. 9(c). All fast Fourier transform (FFT) images in Fig. 9 present two phases which are indicated by green/blue arrows. The dislocation distributions are marked from the inverse fast Fourier transform (IFFT) images which are outlined in the HRTEM images and presented below them. In Figs. 9(a) and 9(b), a small amount of dislocations (yellow dots) exists in the MEA, while the dislocation density is relatively higher inside the Cu layer and near the interface (yellow dashed line). Since the Cu-rich layer is softer than the CoCrNi-rich MEA layer, the dislocations predominantly nucleate inside the Cu-rich layers to accommodate the plastic deformation which results in dislocation pile-ups at the interface between the two layers. In Fig. 9(c), few

dislocations are found in the MEA layers, whereas, a large number of dislocations are gathered inside the thin-Cu nanolayer, leading to pile-up of a high density of dislocations and significant strengthening. Figure 10(a) is the TKD inverse pole figure (IPF) map of the friction-induced laminated structure in the A-45h sample, where a thin-Cu nanolayer with a thickness of about 10 nm lies in the middle. Multiple grains with different orientations are displayed with different colors, and the black regions on the IPF maps correspond to the unindexed or low-confidence index data points. Figure 10(b) is a Kernel Average Misorientation (KAM) map that captures the geometrically necessary dislocations (GNDs) at grain boundaries and interiors [44]. The thin-Cu nanolayer located at the middle is found to exhibit a higher distortion, presumably due to a severe deformation and hence implying the significant Taylor hardening inside these thin-Cu nanolayers. These results are consistent with the high dislocation density presented in Fig. 9(c).

For the A-45h sample, the large amount of sliding friction-induced thin-Cu nanolayers plays a vital role in improving the strength and hardness of the subsurface region. Besides Frank-Read sources, heterogonous interfaces can be also considered as
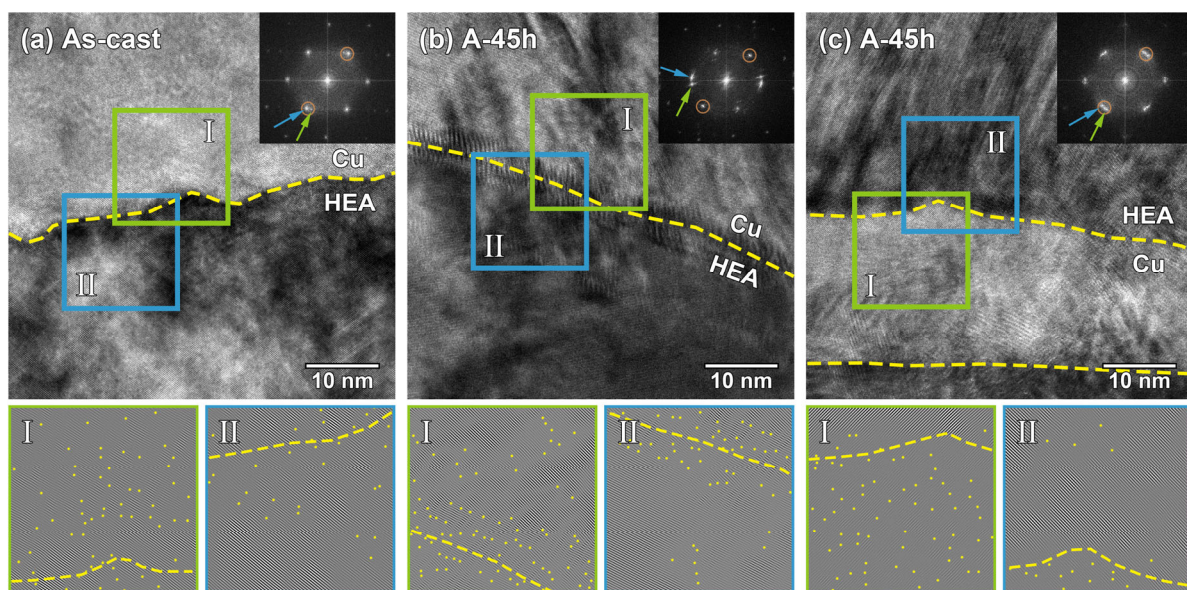

Fig. 9 HRTEM and corresponding FFT images of the interfaces between MEA layers and Cu-rich layers, and the IFFT images of the selected regions (I, II) are displayed below. (a) Interface between thick-Cu nanolayer and MEA nanolayer of the as-cast sample; (b) interface between thick-Cu nanolayer and MEA nanolayer of the A-45h sample; and (c) interface between thin-Cu nanolayer and MEA nanolayer of the A-45h sample.
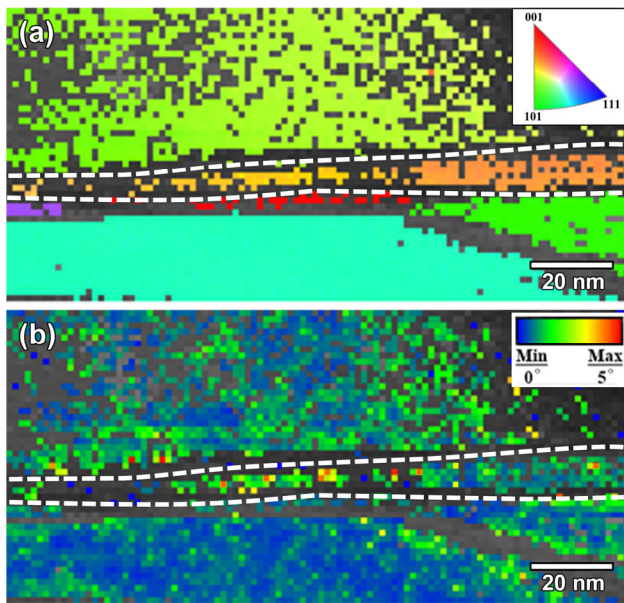
Fig. 10 High magnification TKD map of the friction-induced laminated structure in the A-45h sample. (a) Inverse pole figure (IPF) and crystallographic orientation map and (b) KAM map.

sources of dislocations [45–47]. The interfaces between the Cu-rich layers and the MEA layers, which are considered as preferred nucleating sites, accelerate the generation of extensive dislocations. For nanolaminated materials, the work hardening capacity generally increases with decreasing interface spacing [45, 48, 49]. The deformed thin-Cu nanolayers exhibit excellent hardening capacity because of their unique nanoscale layer thickness. A large amount of dislocations is

assumed to accumulate inside these thin-Cu layers as the deformation continues, which lead to an intensive dislocation-dislocation and dislocation-interface interactions [50, 51]. Once the thin-Cu nanolayers have hardened so much that they are no longer able to provide more space for dislocations to pile-up, dislocations accumulate in the MEA layers and accommodate further plastic deformation. Due to the extensive constraining effect of Cu-rich nanolayers and CoCrNi-rich MEA layers, the subsurface is drastically hardened and wear resistance is significantly improved. In contrast, as the as-cast sample lacks this strengthening of thin-Cu nanolayers, the wear resistance is relatively lower.

We further examined the hardness below the worn surface by AFM indentation to support above hypothesis, as shown in the red dashed box in Fig. 11(a). As can be seen from the hardness distribution mappings, the hardness decreases with an increasing depth from the worn surface. Figure 11(b) plots the variation of hardness as a function of depth from the worn surface. For the as-cast sample, the mean hardness decreases linearly from 1.69 to 1.23 GPa, i.e., a reduction of 27.2%. In contrast, for the A-45h sample, the mean hardness decreases significantly from 1.88 to 0.84 GPa, i.e., a reduction of 55.3%. It is noteworthy that the hardness at the worn surface is higher while the interior hardness is lower of the A-45 sample when compared with the as-cast sample.
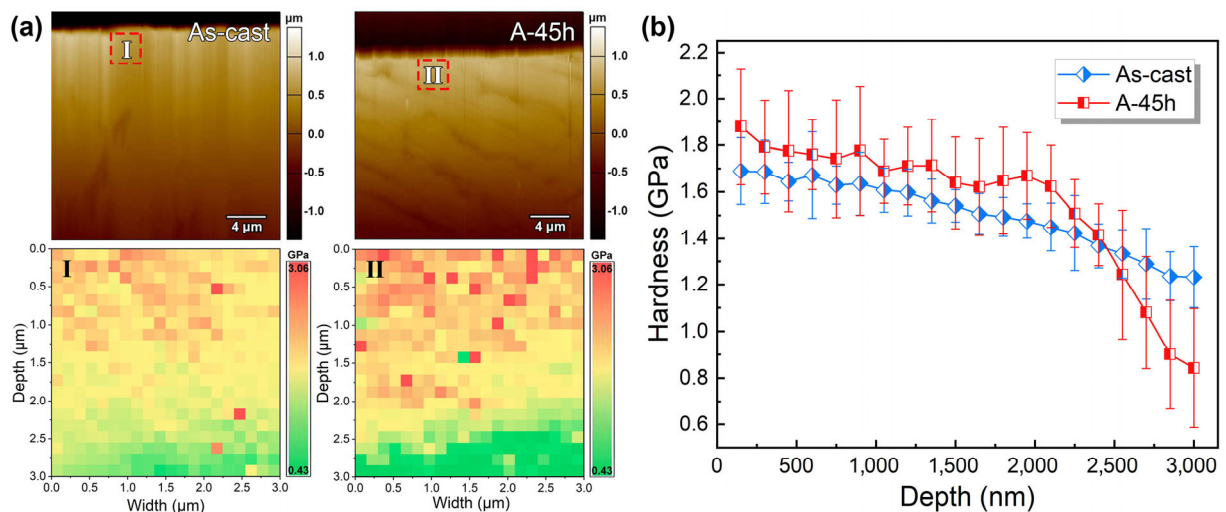

Fig. 11 (a) AFM images of the cross-section beneath the worn surface of the as-cast and the A-45h samples, and the corresponding AFM indentation hardness of the selected region Ⅰ and Ⅱ; (b) nano-hardness as a function of depth beneath the surface for the as-cast and the A-45h samples, respectively.

As the wear influenced deformation region is generally less than 3 μm deep (Figs. 6 and 7), the AFM indentation experiments which covered an area of 3 μm × 3 μm should truly reflect the hardness variety beneath the wear scar. Both samples show an increase of hardness below the worn surface, which is a result of deformation-induced hardening. The interior hardness of the A-45h sample is lower than the as-cast sample, which is consistent with tendency of Vickers hardness as presented in Fig. 3. On the contrary, the hardness of the A-45h sample exhibits a higher value when approaching the worn surface, exceeding that of the as-cast sample. As discussed previously, sliding friction-induced thin-Cu nanolayers in the A-45h sample can promote extensive hardening, which is corroborated here by the AFM results.

Finally, it should be pointed out that apart from the formation of thin-Cu nanolayers, the presence of thick-Cu layers evolved from the inter-dendrites are helpful to form a heterogeneous laminated subsurface, which also contributes to the excellent wear resistance of the A-45h samples. In heterogeneous materials, the strength is provided by hard domains, while the ductility is mainly reserved by soft domains [52, 53]. Under cyclic tribological loading, the soft thick-Cu layers can accommodate the deformation and delay cracking in the subsurface hardened layers. Accordingly, the optimal strength-ductility combination in the A-45h sample may favor a dynamic stable subsurface [54], which minimizes the local fracture and brittle peeling of deformed layers (Fig. 5) during sliding, and leading to the excellent wear performance.

4.2 Tribo-chemical effect

Tuning the element distribution through thermal annealing may contribute to the tribo-chemical effects. Here, the metastable CoCrNiCu HEA (the as-cast sample) was obtained by copper mold casting. Despite the phase separation of Cu at the inter-dendrite region, the dendrite phase still contains supersaturated Cu as diffusion is difficult in HEA [32, 33]. For the A-45h sample, a thermal annealing at 1,100 °C for 45 h can help to precipitate nanoscale Cu phases inside the dendrites. Cu is an easily oxidized element and thus it tends to form oxides to protect the surface from wear during the sliding process [55]. For the

CoCrNiCu HEA, oxidation on the worn surface is confirmed by the EDS analysis presented in Figs. 5(a) and 5(b). To better characterize the oxides formed on the frictional surface, XPS analyses were performed with the results presented in Figs. 5(c)–5(e) that Cu oxides are mainly composed of CuO and Cu_2O. Meanwhile, the A-45h sample shows a higher peak intensity of O^{2-} compared to the as-cast sample, suggesting a higher amount of oxides. In general, the presence of CuO and Cu_2O might be helpful for the formation of glaze layers on the worn surface and could be another main factor for improving the wear resistance [37, 39, 56].

Besides the introduction of easily oxidized Cu, the size of the oxidized debris on the worn surface is also critical for the wear characteristics. For the A-45h sample, a lot of fine debris attached to the worn surface are found in Fig. 12(b). The EDS analysis of this debris is presented in Fig. 12(c). Co, Cr, and Ni are distributed homogeneously in the worn surface, whereas the debris is rich in oxygen and copper as outlined by circles. These nanoscale debris possess a comparable size (50–200 nm) with the Cu-rich precipitates (Fig. 12(b)). Therefore, we conjecture that these nanoscale debris probably originate from the copper precipitates which have undergone severe plastic deformation as well as a chemical reaction. In general, a substantial amount of fine debris is beneficial to be sintered into compact and protective glaze layers attached on the worn surface, leading to a severe-mild wear transition during sliding [23, 55]. Hiratsuka et al. [57] found that large (1–100 mm) wear particles are generated during severe wear of copper, whereas, fine (10–200 nm) wear particles are easily oxidized and generated during mild wear. Yin et al. [24] reported that nanoparticles with 6–20 nm diameter can easily aggregate to the worn surface, thereby forming self-lubricating layers and promoting wear-resistance of the martensitic steel. For present as-cast sample, the debris are loose and large, which are easily detached from the surface and detrimental to the formation of tribolayers due to their severe three-body wear [58]. For the A-45h sample, large amount of scattered debris can be observed underneath the compacted tribolayer in Fig. S2 in the ESM, which evidence that the compacted tribolayers may come
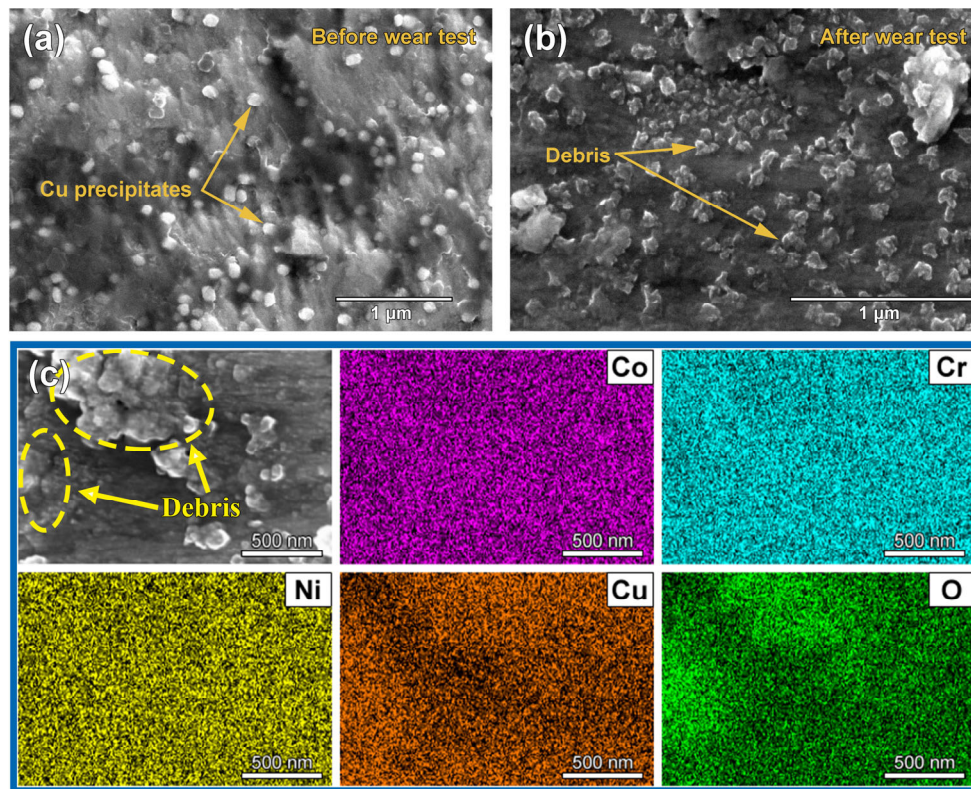
Fig. 12 SEM images of Cu-rich precipitates in the A-45h sample (a) before and (b) after the wear test; (c) EDS mapping of the debris of the A-45h sample after the wear test.

from the sintering of scattered debris during wear process. In conclusion, the Cu-rich nano-precipitates inside the A-45h sample play a vital role in creating a wear-resistant surface. The presence of nano-Cu can accelerate the oxidation process and the change of fine debris into a compacted glaze layer, protecting the surface from further damage.

5   Conclusions

A metastable CoCrNiCu high-entropy alloy (HEA) possessing two FCC phases can be tuned through thermal annealing to enhance its wear resistance. This improvement is ascribed to the formation of a self-organized heterogeneous laminated structure in the subsurface as well as an oxidative tribolayer on the surface during the wear test, as summarized in Fig. 13. Our work suggests and demonstrates strategies for designing wear-resistant HEAs as: Through introducing an *X* element which exhibits positive enthalpy of mixing with the base elements, abundant nano-scale second phase can be precipitated inside the
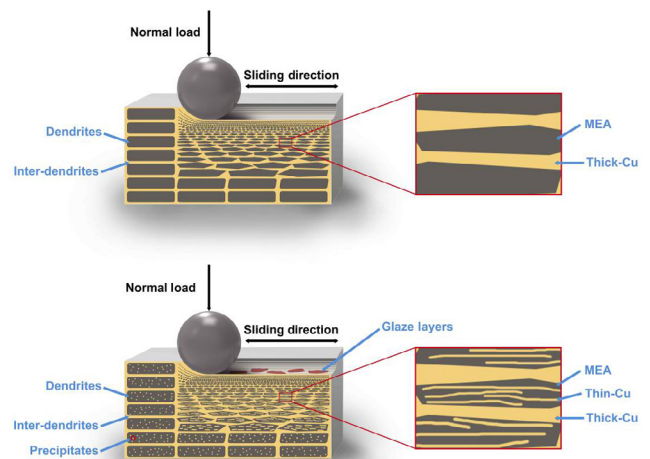

Fig. 13 Mechanisms for the enhanced wear-resistance in the metastable CoCrNiCu HEA.

matrix via thermal annealing. These *X*-rich precipitates should be ductile enough to evolve into a laminated structure during sliding. In addition, the *X* element should be easily oxidized to promote the formation of wear resistant oxide layers. Taking Cu as one example, we draw the following main conclusions:

1) Compared with the as-cast sample, the thermal annealing sample (A-45h sample) has a relative low hardness, but a higher wear resistance can be obtained in this metastable HEA.

2) The sliding friction-induced laminated structure plays a vital role for the wear resistance, as the thin Cu nanolayers can undergo extensive deformation and harden the subsurface.

3) Cu-rich nano-precipitates accelerate the oxidation processes and the evolution of fine debris into compacted tribolayers during the wear process, which in turn protect the surface from further damage.

Acknowledgements

Electronic Supplementary Material: Supplementary material is available in the online version of this article at https://doi.org/10.1007/s40544-022-0606-9.

References

[1] Hua D P, Xia Q S, Wang W, Zhou Q, Li S, Qian D, Shi J Q, Wang H F. Atomistic insights into the deformation mechanism of a CoCrNi medium entropy alloy under nanoindentation. *Int J Plasticity* **142**: 102997 (2021)

[2] Zhang Y, Zuo T T, Tang Z, Gao M C, Dahmen K A, Liaw P K, Lu Z P. Microstructures and properties of high-entropy alloys. *Prog Mater Sci* **61**: 1–93 (2014)

[3] Laplanche G, Kostka A, Reinhart C, Hunfeld J, Eggeler G, George E P. Reasons for the superior mechanical properties of medium-entropy CrCoNi compared to high-entropy CrMnFeCoNi. *Acta Mater* **128**: 292–303 (2017)

[4] Li W, Chou T H, Yang T, Chuang W S, Huang J C, Chen F R. Design of ultrastrong but ductile medium-entropy alloy with controlled precipitations and heterogeneous grain structures. *Appl Mater Today* **23**: 101037 (2021)

[5] Gludovatz B, Hohenwarter A, Thurston K V, Bei H B, Wu Z G, George E P, Ritchie R O. Exceptional damage-tolerance of a medium-entropy alloy CrCoNi at cryogenic temperatures. *Nat Commun* **7**:10602 (2016)

[6] Velişa G, Fan Z, Crespillo M L, Bei H, Weber W J, Zhang Y. Temperature effects on damage evolution in ion-irradiated NiCoCr concentrated solid-solution alloy. *J Alloy Compd* **832**: 154918 (2020)

[7] Wang J Y, Li W H, Yang H L, Huang H, Ji S X, Ruan J M, Liu Z L. Corrosion behavior of CoCrNi medium-entropy alloy compared with 304 stainless steel in H_2SO_4 and NaOH solutions. *Corros Sci* **177:** 108973.1–108973.11 (2020)

[8] Pan S, Zhao C C, Wei P B, Ren F Z. Sliding wear of CoCrNi medium-entropy alloy at elevated temperatures: Wear mechanism transition and subsurface microstructure evolution. *Wear* **440-441**: 203108 (2019)

[9] Erdoğan A, Gök M S, Zeytin S. Analysis of the high-temperature dry sliding behavior of $CoCrFeNiTi_{0.5}Al_x$ high-entropy alloys. *Friction* **8**(1):198–207 (2020)

[10] Du X H, Li W P, Chang H T, Yang T, Duan G S, Wu B L, Huang J C, Chen F R, Liu C T, Chuang W S, Lu Y, Sui M L, Huang E W. Dual heterogeneous structures lead to ultrahigh strength and uniform ductility in a Co–Cr–Ni medium-entropy alloy. *Nat Commun* **11**(1): 2390 (2020)

[11] Yang M X, Zhou L L, Wang C, Jiang P, Yuan F P, Ma E, Wu X L. High impact toughness of CrCoNi medium-entropy alloy at liquid-helium temperature. *Scripta Mater* **172**: 66–71 (2019)

[12] Zhang Z J, Sheng H S, Wang Z J, Gludovatz B, Zhang Z, George E P, Yu Q, Mao S X, Ritchie R O. Dislocation mechanisms and 3D twin architectures generate exceptional strength-ductility-toughness combination in CrCoNi medium-entropy alloy. *Nat Commun* **8**: 14390 (2017)

[13] Miao J, Guo T, Ren J, Zhang A, Su B, Meng J. Optimization of mechanical and tribological properties of FCC CrCoNi multi-principal element alloy with Mo addition. *Vacuum* **149**: 324–330 (2018)

[14] Chuang M, Tsai M, Wang W, Lin S, Yeh J. Microstructure and wear behavior of $Al_xCo_{1.5}CrFeNi_{1.5}Ti_y$ high-entropy alloys. *Acta Mater* **59**(16): 6308–6317 (2011)

[15] Bai L Y, Wan S H, Yi G W, Shan Y, Pham S T, Tieu A K, Li Y, Wang R D. Temperature-mediated tribological characteristics of 40CrNiMoA steel and Inconel 718 alloy during sliding against Si3N4 counterparts. *Friction* **9**(5): 1175–1197 (2020)

[16] Zhou Q, Han W C, Luo D W, Du Y, Xie J Y, Wang X Z, Zou Q G, Zhao X X, Wang H F, Beake B D. Mechanical and tribological properties of Zr–Cu–Ni–Al bulk metallic glasses with dual-phase structure. *Wear* **474–475**: 203880 (2021)

[17] Alvi S, Jarzabek D M, Kohan M G, Hedman D, Jenczyk P, Natile M M, Vomiero A, Akhtar F. Synthesis and mechanical characterization of a CuMoTaWV high-entropy film by magnetron sputtering. *ACS Appl Mater Inter* **12**(18): 21070–21079 (2020)

[18] Vencl A, Bobić I, Bobić B, Jakimovska K, Svoboda P, Kandeva M. Erosive wear properties of ZA-27 alloy-based nanocomposites: Influence of type, amount, and size of nanoparticle reinforcements. *Friction* **7**(4): 340–350 (2019)

[19] Chen X, Han Z, Lu K. Friction and wear reduction in copper with a gradient nano-grained surface layer. *ACS Appl Mater Inter* **10**(16): 13829–13838 (2018)

[20] Zhu W W, Zhao C C, Zhang Y W, Kwok C T, Luan J H, Jiao Z B, Ren F Z. Achieving exceptional wear resistance in a compositionally complex alloy via tuning the interfacial structure and chemistry. *Acta Mater* **188**: 697–710 (2020)

[21] Chu K, Ren F, Zhu W, Zhao C, Bellon P, Averback R S. Sliding wear induced subsurface microstructural evolution in nanocrystalline Nb–Ag binary alloys and its impact on tribological performance. *Wear* **392–393**: 69–76 (2017)

[22] Zheng B C, Li W, Tu X H, Xing J D, Song S C. Effect of interaction between cementite and pearlite on two-body abrasive wear behaviors in white cast iron. *Friction* **9**(6): 1378–1389 (2020)

[23] Sannino A P, Rack H J. Dry sliding wear of discontinuously reinforced aluminum composites review and discussion. *Wear* **189**: 1–19 (1995)

[24] Yin C, Liang Y, Liang Y, Li W, Yang M. Formation of a self-lubricating layer by oxidation and solid-state amorphization of nano-lamellar microstructures during dry sliding wear tests. *Acta Mater* **166**: 208–220 (2019)

[25] Dreano A, Fouvry S, Sao-Joao S, Galipaud J, Guillonneau G. The formation of a cobalt-based glaze layer at high temperature: A layered structure. *Wear* **440–441**: 203101 (2019)

[26] Chen X, Han Z, Li X, Lu K. Lowering coefficient of friction in Cu alloys with stable gradient nanostructures. *Sci Adv* **2**: 1601942 (2016)

[27] Greiner C, Gagel J, Gumbsch P. Solids Under extreme shear: Friction-mediated subsurface structural transformations. *Adv Mater* **31**(26): e1806705 (2019)

[28] Trimby P W, Cao Y, Chen Z B, Han S, Hemker K J, Lian J, Liao X Z, Rottmann P, Samudrala S, Sun J L, et al. Characterizing deformed ultrafine-grained and nanocrystalline materials using transmission Kikuchi diffraction in a scanning electron microscope. *Acta Mater* **62**: 69–80 (2014)

[29] Tran Khac B C, Chung K H. Quantitative assessment of contact and non-contact lateral force calibration methods for atomic force microscopy. *Ultramicroscopy* **161**: 41–50 (2016)

[30] Ken M G, Kempf M, Nix W D. Hardness and modulus of the lamellar microstructure in PST–TiAl studied by nanoindentaion and AFM. *Acta Mater* **49**: 903–911 (2001)

[31] Du Y, Zhou Q, Jia Q, Shi Y D, Wang H F, Wang J. Imparities of shear avalanches dynamic evolution in a metallic glass. *Mater Res Lett* **8**: 357–363 (2020)

[32] Zhou Q, Du Y, Han W C, Ren Y, Zhai H M, Wang H F. Identifying the origin of strain rate sensitivity in a high entropy bulk metallic glass. *Scripta Mater* **164**: 121–125 (2019)

[33] Yang T, Zhao Y L, Fan L, Wei J, Luan J H, Liu W H, Wang C, Jiao Z B, Kai J-J, Liu C T. Control of nanoscale precipitation and elimination of intermediate-temperature embrittlement in multicomponent high-entropy alloys. *Acta Mater* **189**: 47–59 (2020)

[34] Yadav S, Sarkar S, Aggarwal A, Kumar A, Biswas K. Wear and mechanical properties of novel $(CuCrFeTiZn)_{100-x}Pb_x$ high entropy alloy composite via mechanical alloying and spark plasma sintering. *Wear* **410–411**: 93–109 (2018)

[35] Liu X, Zeng M Q, Ma Y, Zhu M. Wear behavior of Al–Sn alloys with different distribution of Sn dispersoids manipulated by mechanical alloying and sintering. *Wear* **265**(11–12): 1857–1863 (2008)

[36] Ren F, Zhu W, Chu K. Fabrication, tribological and corrosion behaviors of ultra-fine grained Co–28Cr–6Mo alloy for biomedical applications. *J Mech Behav Biomed Mater* **60**: 139–147 (2016)

[37] Zhou Q, Ren Y, Du Y, Han W, C Hua D P, Zhai H M, Huang P, Wang F, Wang H F. Identifying the significance of Sn addition on the tribological performance of Ti-based bulk metallic glass composites. *J Alloy Compd* **780**: 671–679 (2019)

[38] Joseph J, Haghdadi N, Shamlaye K, Hodgson P, Barnett M, Fabijanic D. The sliding wear behaviour of CoCrFeMnNi

and Al$_x$CoCrFeNi high entropy alloys at elevated temperatures. *Wear* **428–429**: 32–44 (2019)

[39] Lehmann J S, Schwaiger R, Rinke M, Greiner C. How tribo-oxidation alters the tribological properties of copper and its oxides. *Adv Mater Inter* **8**(1): 2001673 (2020)

[40] Archard J F. Contact and Rubbing of Flat Surfaces. *J Appl Phys* **24**(8): 981–988 (1953)

[41] R M, Bellon P, Averback R S. Wear Resistance of Cu/Ag Multilayers: A Microscopic Study. *ACS Appl Mater Inter* **10**(17):15288–15297 (2018)

[42] Cheng Z, Yang L, Huang Z K, Wan T, Zhu M Y, Ren F Z. Achieving low wear in a μ-phase reinforced high-entropy alloy and associated subsurface microstructure evolution. *Wear* **474-475**: 203755 (2021)

[43] Zhang Z, Lin G, Zhang S, Zhou J. Effects of Ce on microstructure and mechanical properties of pure copper. *Mater Sci Eng A* **457**(1–2): 313–318 (2007)

[44] Clair A, Foucault M, Calonne O, Lacroute Y, Markey L, Salazar M, Vignal V, Finot E. Strain mapping near a triple junction in strained Ni-based alloy using EBSD and biaxial nanogauges. *Acta Mater* **59**(8): 3116–3123 (2011)

[45] Huang C X, Wang Y F, Ma X L, Yin S, Höppel H W, Göken M, Wu X L, Gao H J, Zhu Y T. Interface affected zone for optimal strength and ductility in heterogeneous laminate. *Mater Today* **21**(7): 713–719 (2018)

[46] Zhou Q, Li Y, Wang F, Huang P, Lu T J, Xu K W. Length-scale-dependent deformation mechanism of Cu/*X* (*X* = Ru, W) multilayer thin films. *Mater Sci Eng A* **664**: 206–214 (2016)

[47] Luo D W, Zhou Q, Ye W T, Ren Y, Greiner C, He Y X, Wang H F. Design and characterization of self-lubricating refractory high entropy alloy-based multilayered films. *ACS Appl Mater Inter* **13**: 55712–55725 (2021)

[48] Hua D P, Wang W, Luo D W, Zhou Q, Li S, Shi J Q, Fu M S, Wang H F. Molecular dynamics simulation of the tribological performance of amorphous/amorphous nano-laminates. *J Mater Sci Technol* **105**: 226–236 (2022)

[49] Pang J Y, Zhang H W, Zhang L, Zhu Z W, Fu H, Li H, Wang A M, Li Z K, Zhang H F. Ductile Ti$_{1.5}$ZrNbAl$_{0.3}$ refractory high entropy alloy with high specific strength. *Mater Lett* **290**: 129428–129428 (2021)

[50] Zhao Y F, Zhang J Y, Wang Y Q, Wu K, Liu G, Sun J. Unusual plastic deformation behavior of nanotwinned Cu/high entropy alloy FeCoCrNi nanolaminates. *Nanoscale* **11**(23): 11340–1150 (2019)

[51] Moon J, Tabachnikova E, Shumilin S, Hryhorova T, Estrin Y, Brechtl J, et al. Unraveling the discontinuous plastic flow of a Co–Cr–Fe–Ni–Mo multiprincipal-element alloy at deep cryogenic temperatures. *Phys Rev Mater* **5**(8): 083601 (2021)

[52] Hasan M N, Liu Y F, An X H, Gu J, Song M, Cao Y, Li Y S, Zhu Y T, Liao X Z. Simultaneously enhancing strength and ductility of a high-entropy alloy via gradient hierarchical microstructures. *Inter J Plasticity* **123**: 178–195 (2019)

[53] Gao B, Lai Q Q, Cao Y, Hu R, Xiao L R, Pan Z Y, Liang N N, Li Y S, Sha G, Liu M P, Zhou H, Wu X L, Zhu Y T. Ultrastrong low-carbon nanosteel produced byheterostructure and interstitial mediated warm rolling. *Sci Adv* **6**: 8169–8192 (2020)

[54] Lu Z C, Zeng M Q, Gao Y, Zhu M. Minimizing tribolayer damage by strength–ductility matching in dual-scale structured Al–Sn alloys: A mechanism for improving wear performance. *Wear* **304**(1–2): 162–172 (2013)

[55] Verma A, Tarate P, Abhyankar A C, Mohape M R, Gowtam D S, Deshmukh V P, Shanmugasundaram T. High temperature wear in CoCrFeNiCu$_x$ high entropy alloys: The role of Cu. *Scripta Mater* **161**: 28–31 (2019)

[56] Xin B, Yu Y, Zhou J, Wang L, Ren S. Effect of copper molybdate on the lubricating properties of NiCrAlY laser clad coating at elevated temperatures. *Surf Coat Tech* **313**: 328–336 (2017)

[57] Hiratsuka K, Muramoto K. Role of wear particles in severe–mild wear transition. *Wear* **259**(1–6): 467–476 (2005)

[58] Ghosh D, Subhash G, Radhakrishnan R, Sudarshan T S. Scratch-induced microplasticity and microcracking in zirconium diboride–silicon carbide composite. *Acta Mater* **56**(13): 3011–3022 (2008)

Yue REN. He received his bachelor and master degrees in School of Materials Science and Engineering of Northwestern Polytechnical University, China, in 2017 and 2020, respectively. Meanwhile, he was a joint mater student during his master degree in Laboratoire de Mécanique des Contacts et des Structures (LaMCoS) from Institut National des Sciences Appliquées de Lyon, France. From 2020, he is a Ph.D. candidate in the State Key Laboratory of Solidification Processing and the Center of Advanced Lubrication and Seal Materials at Northwestern Polytechnical University. His research interests include metallic alloy, cryogenics, and tribology.

Qing ZHOU. He received his Ph.D. degree in Xi'an Jiaotong University, China, in 2017, majoring in materials science and engineering. Then he has worked at Northwestern Polytechnical University as an associate professor. From 2021, he worked at Karlsruhe Institute of Technology (KIT) as a postdoctor. His research areas cover design, fabrication, and characterization of high-performance alloy materials, modeling and simulation of tribological behaviors of metal composites, etc.

Haifeng WANG. He received his Ph.D. degree in material processing engineering from Northwestern Polytechnical University, China, in 2010. He joined the State Key Laboratory of Solidification Processing at Northwestern Polytechnical University from 2010 and the Center of Advanced Lubrication and Seal Materials from 2017. Prof. Haifeng Wang worked as a fellow of Alexander von Humboldt Foundation during 2011–2013, and a visiting scholar during 2014–2015 in Institut für Materialphysik im Weltraum at Deutsches Zentrum für Luft-und Raumfahrt. His research areas cover metal-based and ceramic based wear resistance and lubrication materials, non-equilibrium theory of solidification and solid-state phase-transformation, and preparation of non-equilibrium materials including bulk metallic glass and its composite, etc.